Electronic Supplementary Material (ESI) for Catalysis Science & Technology.
This journal is © The Royal Society of Chemistry 2020

Supporting information

Ru nanoparticles encapsulated in ZIFs-derived porous N-doped hierarchical carbon nanofibers for enhanced hydrogen evolution reaction

Libing Fan,[a,b] Tian Meng,[b,c] Qun Li,[b,c] Dewen Wang,[b,c]Zhicai Xing,*[,b] Erkang Wang,*[,a,b,c] and Xiurong Yang*[,b,c]

[a]College of Chemistry, Jilin University, Changchun 130012, China

[b]State Key Laboratory of Electroanalytical Chemistry, Changchun Institute of Applied Chemistry, Chinese Academy of Sciences, Changchun 130022, Jilin, China

[c]School of Applied Chemistry and Engineering, University of Science and Technology of China, Hefei 230026, China

*E-mail: xingzc@ciac.ac.cn; ekwang@ciac.ac.cn; xryang@ciac.ac.cn

Tel: +86-0431-85262056.

Measurement of electrochemically active surface area (ECSA)

The underpotential deposition of copper (Cu-UPD) was used to determine the ECSA of different metal-containing electrocatalysts. 5 μL of ES-Ru-ZIF-900 catalyst ink dropped on the polished glassy carbon electrode (GCE). The dried GCE was firstly cycled in 0.5 M H_2SO_4 between 0 to 0.8 V *vs* RHE with a scan rate of 10 mV s^{-1} and acted as a baseline. Then, the solution was changed to 0.5 M H_2SO_4 and 20 mM $CuSO_4$ for Cu-UPD. During the reaction process, overpotential deposition (OPD) was also occurred. Thus, the mixed solution of 0.5 M H_2SO_4, 20 mM $CuSO_4$ and 60 mM NaCl was used to separate the UPD and OPD peaks owing to the fact that the Cl^- can be quick adsorption on the Cu UPD adlayer and inhibition of the Cu OPD.

Hydrogen evolution reaction (HER) mechanisms

HER is a two-step two-electron electrochemical process taking place on the surface of an electrode that generates gaseous hydrogen. Commonly, the accepted HER reaction mechanisms in alkaline solution follows the classical Volmer-Heyrovsky process or the Volmer-Tafel process, which are as follows.

step 1: Volmer reaction (electrochemical hydrogen adsorption)

$$M + H_2O + e^- \rightleftharpoons M\text{-}H^* + OH^- \text{ (b: ~120 mV dec}^{-1}\text{)} \quad (1)$$

step 2: Heyrovsky reaction (electrochemical desorption):

$$M\text{-}H^* + H_2O + e^- \rightleftharpoons M + OH^- + H_2 \text{ (b: ~40 mV dec}^{-1}\text{)} \quad (2)$$

Or Tafel reaction (chemical desorption):

$$2\ M\text{-}H^* \rightleftharpoons 2\ M + H_2 \text{ (b: ~30 mV dec}^{-1}\text{)} \quad (3)$$

Where H* represents the hydrogen atom chemically adsorbed on an active site of the electrode surface (M).

Calculation of turn over frequency (TOF)

The following equation was used to calculate the TOF values of the electrocatalysts:

$$\mathrm{TOF} = I/2nF \qquad (4)$$

where I, n, and F are corresponding to the current (A) during the LSV measurement in 1.0 M KOH, the number of actives sites (mol) and the Faraday constant (96485 C/mol), respectively. The factor 2 indicates the mole of electrons consumed for evolving one mole of hydrogen molecule from water.

The number of actives sites of the electrocatalysts was determined as follows. The CV curves were recorded in the potential range from -0.2 to 0.65 V vs RHE with a scan rate of 50 mV s^{-1} in 1.0 M PBS (pH = 7). Under the given geometric area, the number of active sites n is proportional to the total charge Q which can be calculated by integrating the obtained CV curves, and then the n can be acquired based on the equation (5). Note: we assumed that all the metallic Ru participated in the electrochemical HER process for the various electrocatalysts.

$$n = Q/2F \qquad (5)$$

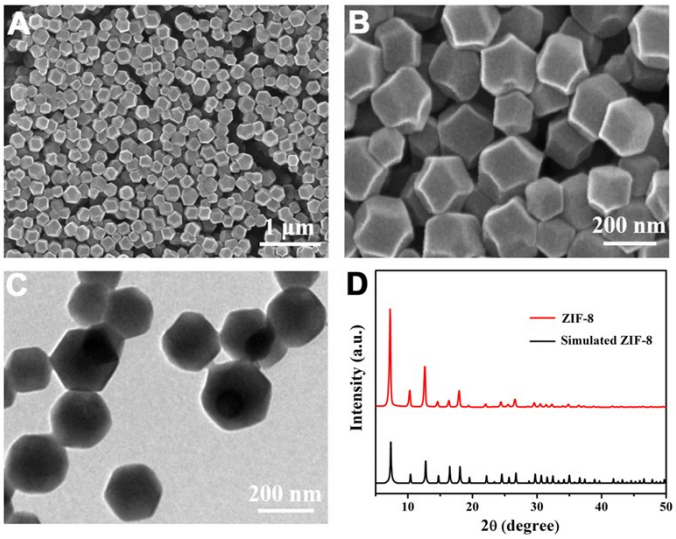

Fig. S1 (A, B) SEM, (C) TEM images and (D) XRD pattern of ZIF-8.

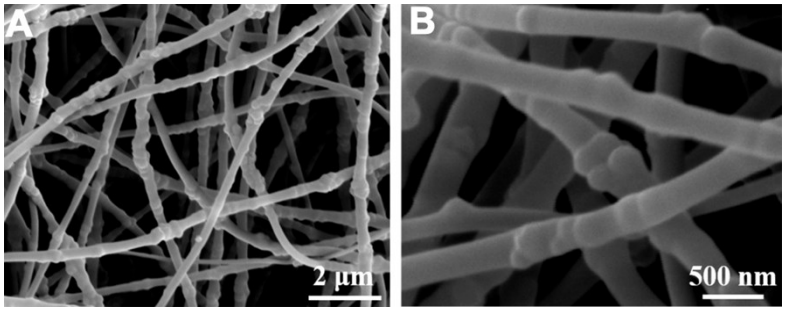

Fig. S2 (A) Low- and (B) high-magnification SEM images of $RuCl_3$/ZIF-8/PAN NFs.

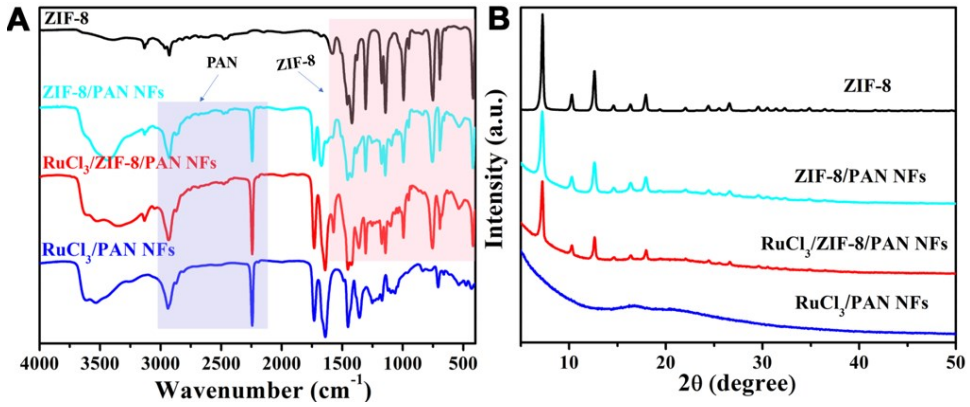

Fig. S3 (A) FTIR spectra and (B) XRD patterns of ZIF-8, ZIF-8/PAN NFs, $RuCl_3$/ZIF-8/PAN NFs and $RuCl_3$/PAN NFs.

The peaks in purple region of the FTIR spectra are mainly from PAN polymer, while the peaks in the pink region are mainly from ZIF-8.[1]

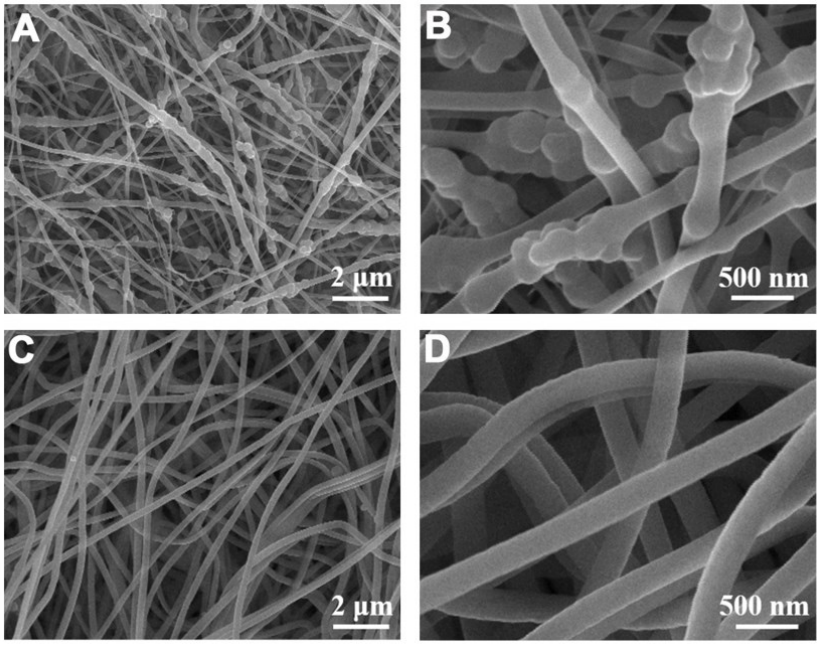

Fig. S4 SEM images of (A, B) ZIF-8/PAN NFs and (C, D) $RuCl_3$/PAN NFs.

These two types of NFs display completely different morphologies: For ZIF-8/PAN NFs, the large ZIF-8 particles are agglomerated in the NFs, making the size of the NFs significantly uneven. But for $RuCl_3$/PAN NFs, the surface is smooth and the morphology is extremely uniform without the presence of ZIF-8.

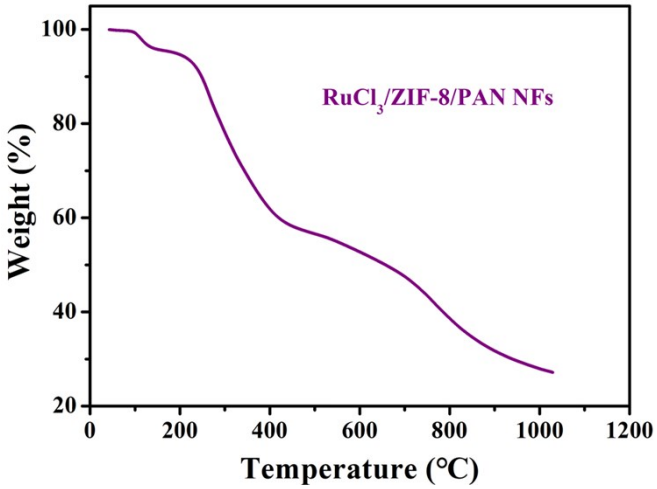

Fig. S5 TGA curve of the $RuCl_3$/ZIF-8/PAN NFs.

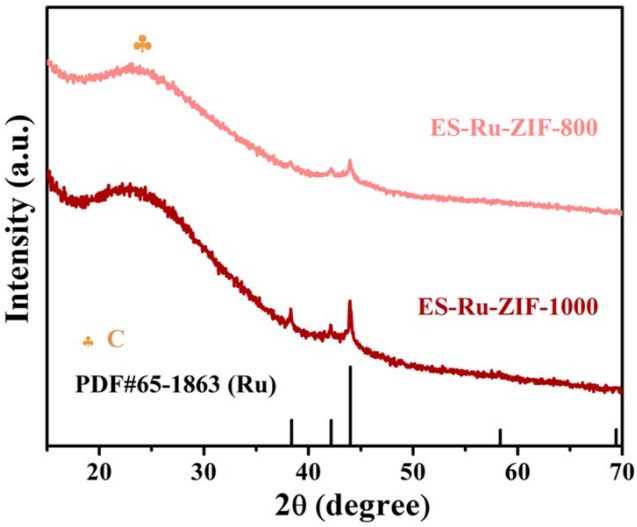

Fig. S6 XRD patterns of ES-Ru-ZIF-800 and ES-Ru-ZIF-1000.

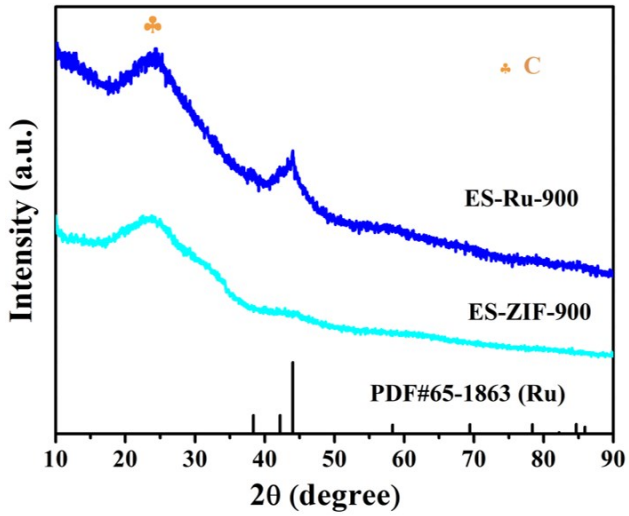

Fig. S7 XRD patterns of ES-Ru-900 and ES-ZIF-900.

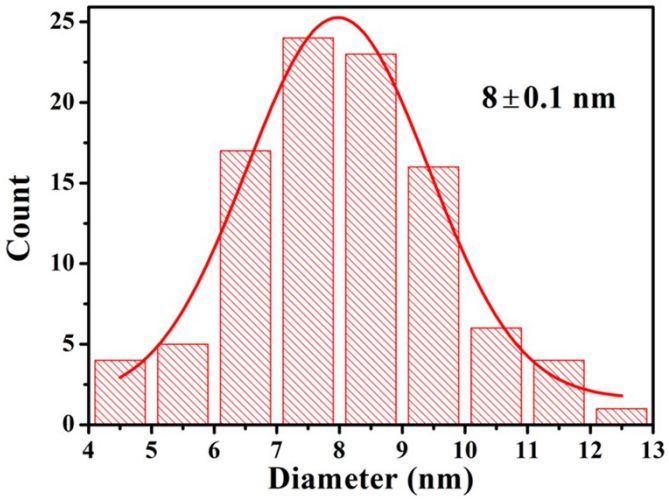

Fig. S8 Histogram of the diameter distribution of Ru NPs in ES-Ru-ZIF-900.

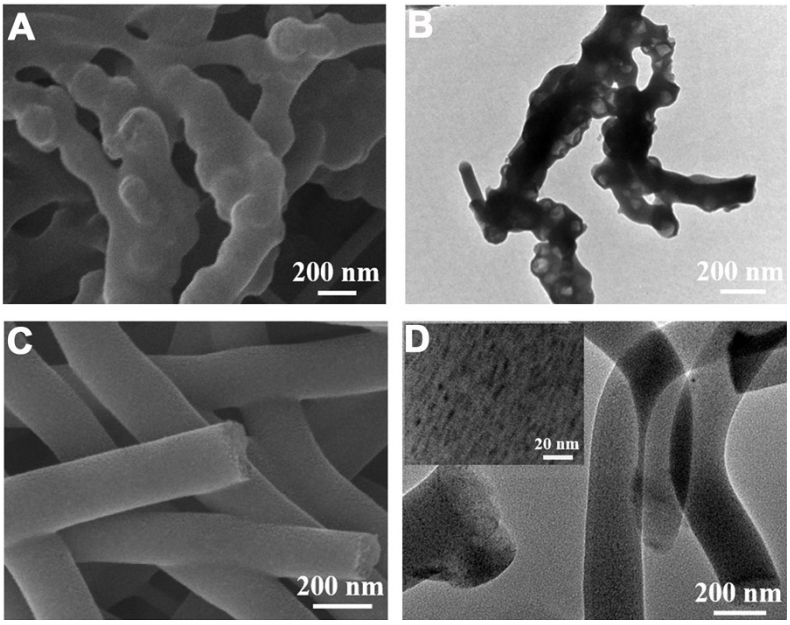

Fig. S9 SEM images of (A) ES-ZIF-900 and (C) ES-Ru-900, TEM images of (B) ES-ZIF-900 and (D) ES-Ru-900.

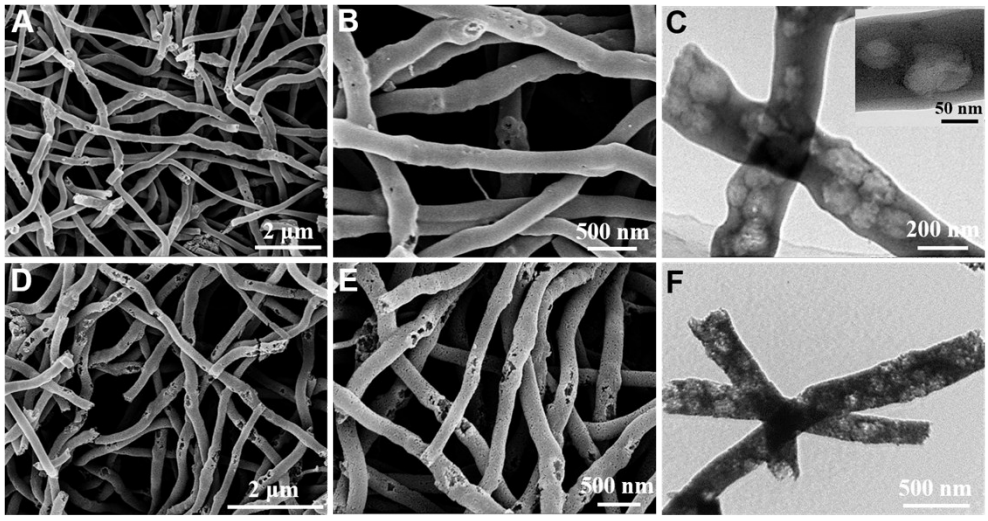

Fig. S10 SEM images of (A, B) ES-Ru-ZIF-800 and (D, E) ES-Ru-ZIF-1000, TEM images of (C) ES-Ru-ZIF-800 and (F) ES-Ru-ZIF-1000.

Compared to ES-Ru-ZIF-900, the fiber surface of ES-Ru-ZIF-800 is almost unbroken and only leaves the hollow structure inside the fibers. Upon increasing the temperature to 1000 °C, accompy with the further pyrolysis of ZIF-8 and PAN polymer, lots of holes and gaps appear on the surface of the fibers and the particles agglomeration become more severe in ES-Ru-ZIF-1000.

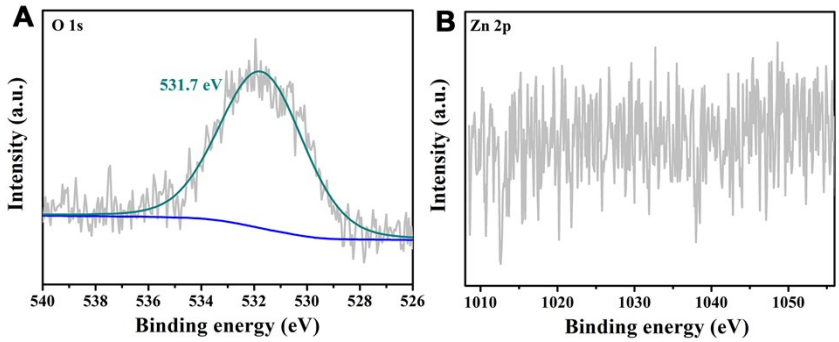

Fig. S11 High-resolution XPS spectra of (A) O 1s and (B) Zn 2p for ES-Ru-ZIF-900.

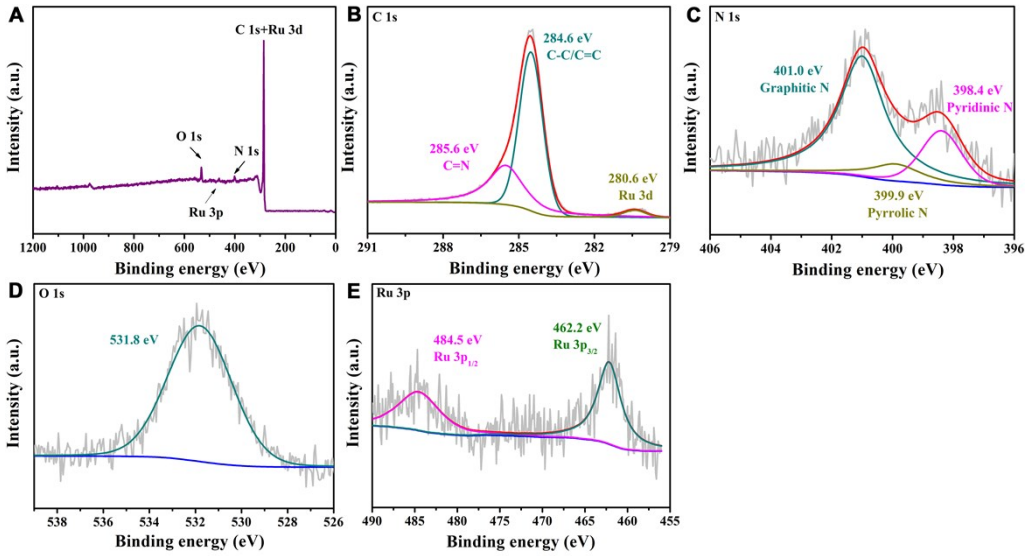

Fig. S12 XPS survey spectrum (A), high-resolution XPS spectra of (B) C 1s, (C) N 1s, (D) O 1s and (E) Ru 3p for ES-Ru-900.

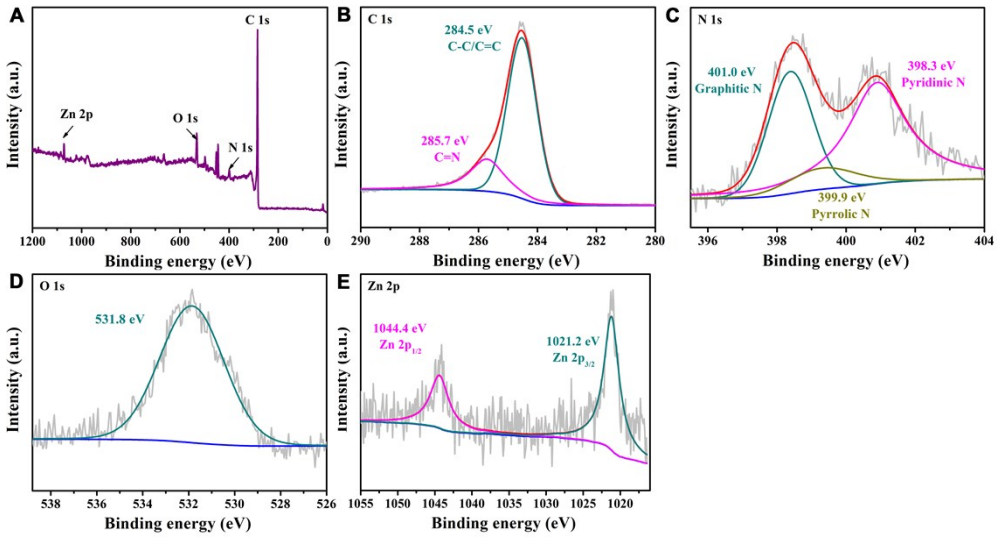

Fig. S13 XPS survey spectrum (A), high-resolution XPS spectra of (B) C 1s, (C) N 1s, (D) O 1s and (E) Zn 2p for ES-ZIF-900.

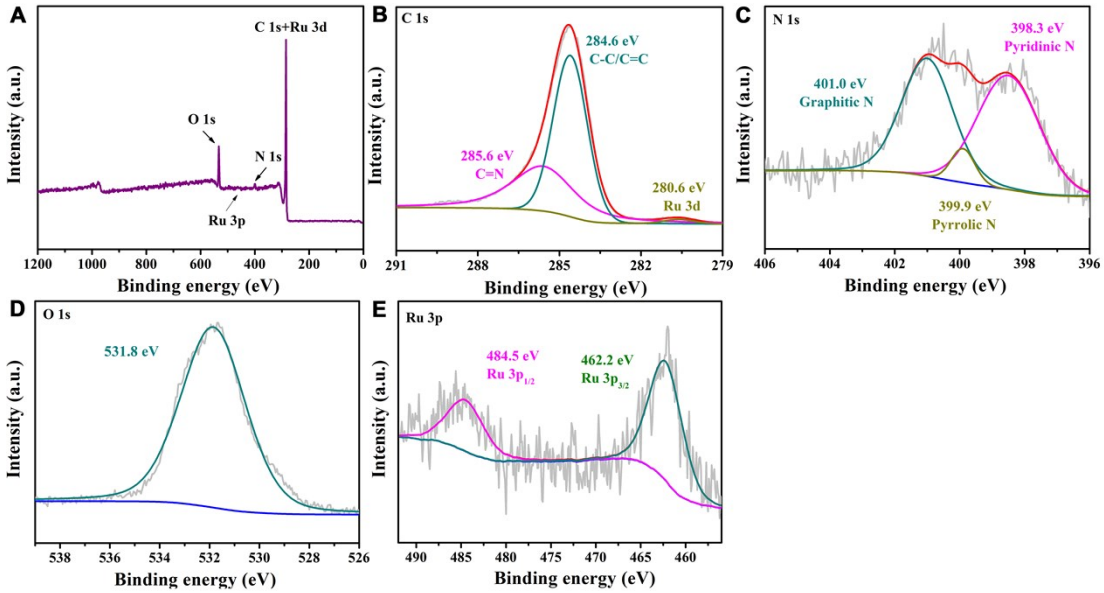

Fig. S14 XPS survey spectrum (A), high-resolution XPS spectra of (B) C 1s, (C) N 1s, (D) O 1s and (E) Ru 3p for ES-Ru-ZIF-800.

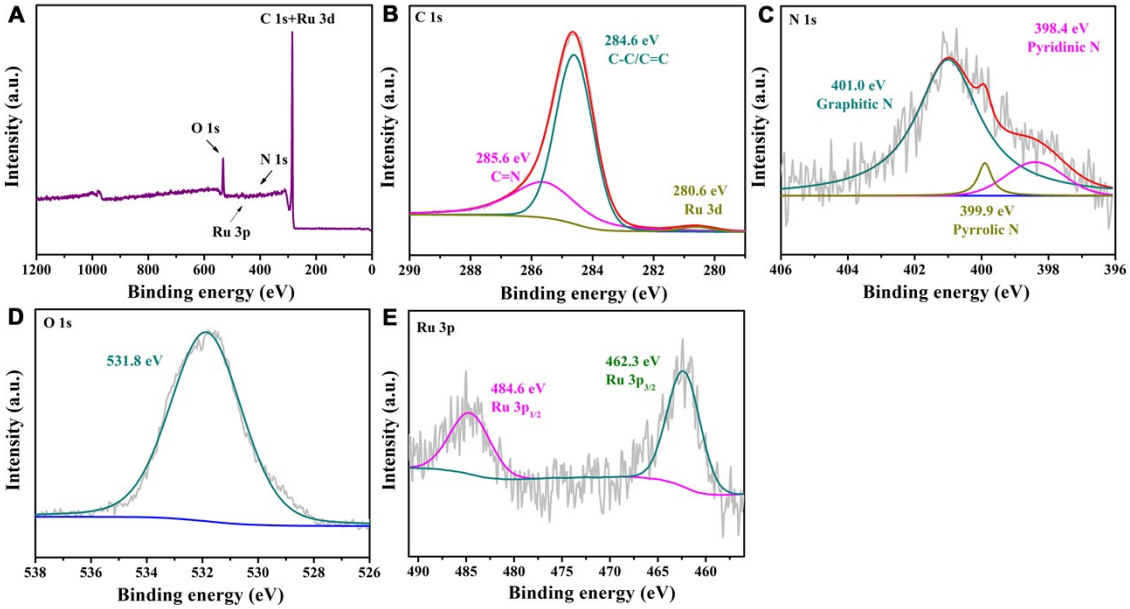

Fig. S15 XPS survey spectrum (A), high-resolution XPS spectra of (B) C 1s, (C) N 1s, (D) O 1s and (E) Ru 3p for ES-Ru-ZIF-1000.

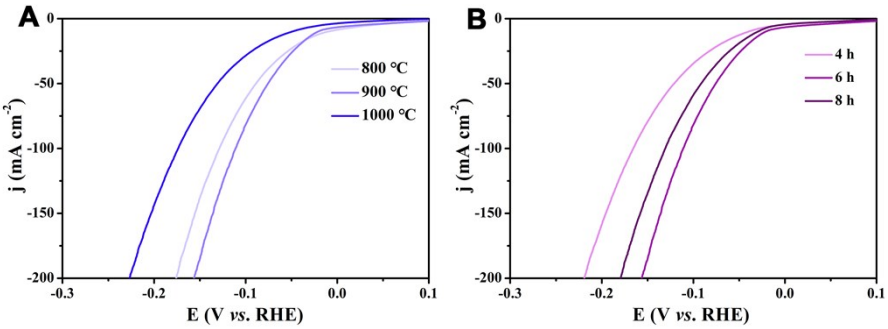

Fig. S16 Polarization curves of ES-Ru-ZIF prepared at different calcination (A) temperatures and (B) times.

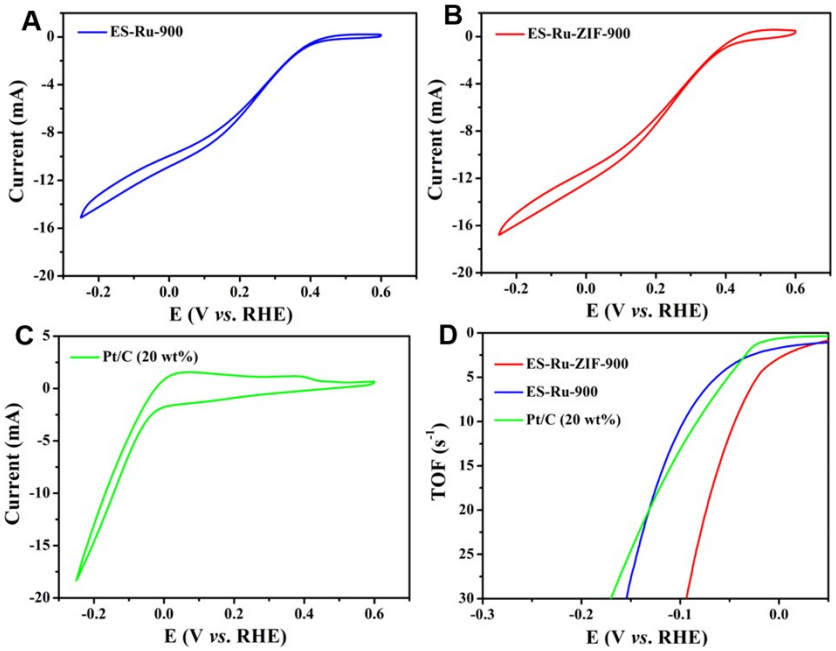

Fig. S17 CVs of (A) ES-Ru-900, (B) ES-Ru-ZIF-900 and (C) Pt/C (20 wt%) in 1.0 M PBS (pH = 7) with a scan rate of 50 mV s^{-1}. (D) Calculated TOFs for ES-Ru-900, ES-Ru-ZIF-900 and Pt/C (20 wt%) in 1.0 M KOH.

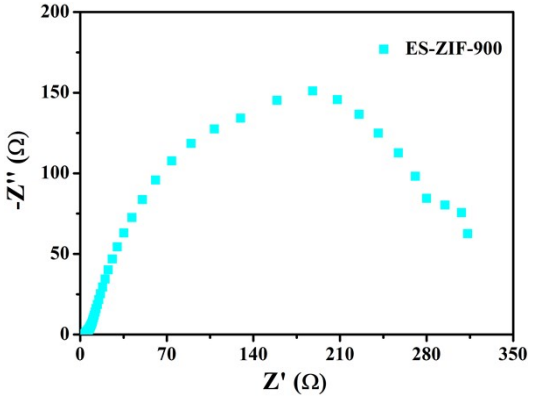

Fig. S18 Nyquist plots of the ES-ZIF-900.

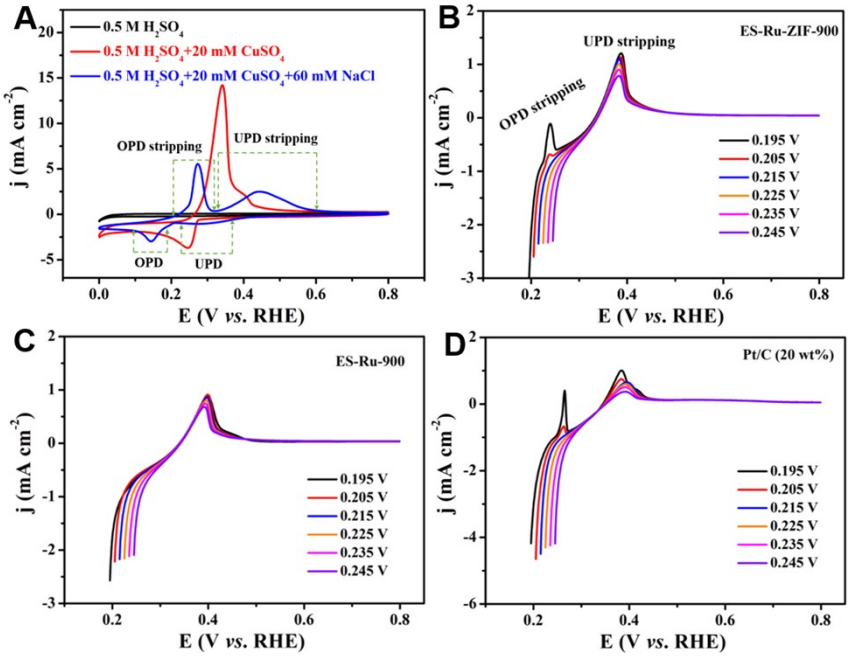

Fig. S19 (A) The current-voltage scan for ES-Ru-ZIF-900 in different solutions. LSV curves of (B) ES-Ru-ZIF-900, (C) ES-Ru-900 and (D) Pt/C (20 wt%) under different initial voltages (scan rates: 2 mV s^{-1}).

As exhibited in Fig. S19A, the CV curve of ES-Ru-ZIF-900 tested in 0.5 M H_2SO_4 acted as a baseline (without any oxidation or reduction peaks). After measuring in the 0.5 M H_2SO_4 + 20 mM $CuSO_4$ solution, only one reduction peak or oxidation peak appeared, meaning that the UPD and overpotential deposition (OPD) are overlapped. Cl^- has been proven to be efficient for the separation of the UPD and OPD peaks *via* quick adsorption on the Cu UPD adlayer and inhibition of the Cu OPD. After addition of Cl^-, the regions for OPD, UPD and their stripping peaks are clearly observed. On the basis of the CV results measured in 0.5 M H_2SO_4 + 20 mM $CuSO_4$ + 60 mM NaCl solution, we then selected a series of initial underpotential points from 0.195 V to 0.245 V to test the LSV data of the stripping of deposited Cu. As seen in Fig. S19B-D, there is no obvious OPD stripping peak involved when the Cu is deposited at the voltage of 0.215 V or above. Thus, the curve at 0.215 V is used to extract the charge quantity (Q_{Cu}). The ECSA of the metal-containing electrocatalysts could be proportional to the stripping charge of Cu-UPD adlayer according to the following equation (6)[2]:

$$ECSA\ (cm^2 / g_{metal}) = Q_{Cu} / (M_{metal} \times 420\ \mu C\ cm^{-2}) \qquad (6)$$

Where M_{metal} (g) is the loading of metal content on the working electrode, 420 μC cm^{-2} is the value for a saturated Cu-UPD monolayer formation on active metal sites. The values of Q_{Cu} (C) is obtained from the LSV curves[3, 4].

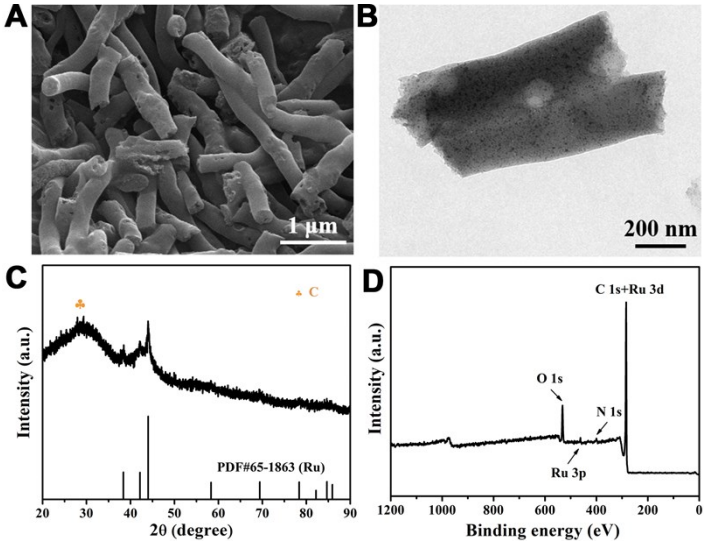

Fig. S20 (A) SEM image, (B) TEM image, (C) XRD pattern and (D) XPS survey spectrum for ES-Ru-ZIF-900 after the stability test.

Table S1 Porosity parameters of the samples prepared in this work.

Samples	Total pore volume (cm^3 g^{-1})	Average pore diameter (nm)
ES-Ru-ZIF-900	0.712	3.815
ES-Ru-900	0.523	3.407
ES-ZIF-900	0.896	3.821

Table S2 ICP-OES results of ES-Ru-ZIF-T.

Samples	Ru content (wt %)	Zn content (wt %)
ES-Ru-ZIF-800	8.2	0.36
ES-Ru-ZIF-900	8.5	0.17
ES-Ru-ZIF-1000	8.1	0.03

Table S3 Comparison of the HER activity for ES-Ru-ZIF-900 with other recently reported catalysts in alkaline medium.

Catalysts	Mass loading (mg cm^{-2})	Overpotential at 10 mA cm^{-2} (mV)	Tafel slope (mV dec^{-1})	References
ES-Ru-ZIF-900	0.157	21	64	This work
C_3N_4-Ru-F	0.153	140	57	J. Mater. Chem. A 2017, 5, 18261
C_3N_4-rGO-Ru	0.153	80	56	ChemSusChem 2018, 11, 130
Ru-NC-2	0.86	81	88	Chem. Commun 2018, 54, 13076
Sr_2RuO_4	0.232	61	51	Nat. Commun. 2019, 10, 149
Ru-MoS_2/CC	~ 12.44	41	114	Appl. Catal. B Environ. 2019, 249, 91
Ru_1Ni_1-NCNFs	0.612	35	30	Adv. Sci. 2019, 1901833
NiO/Ru@Ni	not given	39	75	J. Mater. Chem. A 2019, 7, 2344
Ru-RuO_2/CNT	0.8	12	30	Nano energy 2019, 61, 576
Ni-MOF@Pt	0.2	102	88	Nano lett. 2019, 19, 8447
CDs/Pt-PANI-4	not given	56	58	Appl. Catal. B Environ. 2019, 257, 117905
$PtRu/CC_{1500}$	Pt: 1.6 μg cm^{-2}	19	28	J. Mater. Chem. A 2020, 8, 2090
Rh nanosheets	not given	37	74.7	Chem. Mater. 2017, 29, 5009

References

1. C. H. Wang, C. Liu, J. S. Li, X. Y. Sun, J. Y. Shen, W. Q. Han and L. J. Wang., *Chem. Commun.*, 2017, **53**: 1751-1754.
2. L. W. Xing, H. Y. Gao, G. T. Hai, Z. P. Tao, J. Zhao, D. D. Jia, X. Chen, M. Y. Han, S. Hong, L. R. Zheng, X. B. Huang, W. J. Dong, G. Wang and X. T. Shu. *J. Mater. Chem. A*, 2020, **8**, 3203-3210.
3. X. L. Yang, A. Y. Lu, Y. H. Zhu, M. N. Hedhili, S. X. Min, K. W. Huang, Y. Han and L. J. Li. *Nano Energy*, 2015, **15**, 634-641.
4. J. Wang, Z. Z. Wei, S. J. Mao, H. R. Li and Y. Wang. *Energy Environ. Sci.*, 2018, **11**, 800-806.